PHYSICAL REVIEW B **90**, 035137 (2014)

Magnetic excitations in a spin-orbit-coupled d^4 Mott insulator on the square lattice

Alireza Akbari and Giniyat Khaliullin
Max-Planck-Institut für Festkörperforschung, Heisenbergstrasse 1, D-70569 Stuttgart, Germany

(Received 16 May 2014; revised manuscript received 15 July 2014; published 28 July 2014)

We study the magnetic order and excitations in strong spin-orbit-coupled, Van Vleck–type, d^4 Mott insulators on a square lattice. Extending the previous work, we include the tetragonal crystal-field splitting and explore its effects on the magnetic phase diagram and magnon spectra. Two different ordered phases, with in-plane and out-of-plane orientations of the staggered moments, are found for the higher and lower values of the crystal-field splitting, respectively. The magnetic excitation spectra for paramagnetic and magnetically ordered phases are calculated and discussed in the context of a candidate spin-orbit d^4 Mott insulator, Ca_2RuO_4.

DOI: 10.1103/PhysRevB.90.035137 PACS number(s): 75.10.Jm, 75.25.Dk, 75.30.Et

I. INTRODUCTION

In a solid, fivefold orbital degeneracy of a d electron level is lifted by the crystal-field potential as well as by covalency effects. In the case of local cubic symmetry, two subsets of d orbitals with twofold e_g and threefold t_{2g} symmetry, separated by a large energy of the order of $10Dq \sim 2$–3 eV, are formed. The remaining degeneracy of orbitals, which adds up to that of spin, has to be lifted one way or another, involving the dynamical Jahn-Teller effect and interionic exchange interactions. If the latter mechanism dominates, the spin and orbital degrees of freedom strongly couple to each other and are described by a family of so-called Kugel-Khomskii-type models [1].

General behavior of Kugel-Khomskii Hamiltonians is very complex because of the frustrated nature of orbital interactions, particularly in the case of t_{2g} orbitals, where the higher degeneracy enhances quantum effects [2,3]. In addition to that, the t_{2g} triplet has an unquenched orbital angular momentum L, and relativistic spin-orbit coupling (SOC) $\lambda(\boldsymbol{S}\cdot\boldsymbol{L})$ is active. When λ is comparable to the strength of the exchange interactions, spin-orbit-coupling effects become of a nonperturbative nature. In that case, it is more convenient to represent the spin-orbital exchange Hamiltonians in terms of ionic multiplets in which SOC is already included [4]. Often, it is sufficient to keep the lowest-lying ionic multiplet with $2\tilde{S}+1$ degeneracy; this results in effective "pseudospin $\tilde{S}$" Hamiltonians describing low-energy magnetic properties of a material.

By construction, pseudospins $\tilde{S}$ inherit the spatial shape and bond-directional nature of orbitals and their interactions [3]. Thus, the pseudospin Hamiltonians may strongly deviate from a conventional, spin-isotropic Heisenberg model, even in the simplest case of just twofold Kramers degeneracy with $\tilde{S}=1/2$. As an example, exchange interactions between t_{2g}^5 ions with pseudospins $\tilde{S}=1/2$ obtain a large Ising term with an unusual bond-dependent alternation of the "'Ising axes" [3,5,6], leading to unconventional magnetic states. The pseudospin Hamiltonians for $\tilde{S}>1/2$ also receive strong biquadratic and multipolar interactions [7,8]. Experimental studies of the iridium oxides hosting pseudospin physics [9–11] have boosted general interest in strong spin-orbit-coupled magnetism (see Ref. [12] for a recent review).

It may happen that the lowest spin-orbit ionic state has no degeneracy, $\tilde{S}=0$, and hence it is nonmagnetic. Such is the case for transition-metal ions with the t_{2g}^4 configuration, where the spin $S=1$ and orbital $L=1$ moments form a singlet ground state [13]. Compounds with such nominally nonmagnetic ("Van Vleck–type") ions may still undergo magnetic transitions due to mixing of the ground state $\tilde{S}=0$ level with higher-lying $\tilde{S}=1,2$ multiplets by virtue of intersite exchange interactions [14]. Because of SOC, the transitions between multiplets with different $\tilde{S}$ are magnetically active. In a solid, they become dispersive bands and have been observed in cobalt [15,16] and iridium [11] oxides. Magnetic order in systems with $\tilde{S}=0$ can thus be viewed as a Bose condensation of the excitonic $\tilde{S}=1$ band. A hallmark of such magnetism is the presence of the soft amplitude mode [17], corresponding here to the length fluctuations of the total angular momentum $\tilde{\boldsymbol{S}}=\boldsymbol{S}+\boldsymbol{L}$, in addition to conventional spin waves.

A theory of the exchange interactions and excitonic magnetism in Van Vleck–type t_{2g}^4 systems has been developed recently in Ref. [14], and ruthenium oxide (Ca_2RuO_4) was suggested as a possible candidate material based on the experimental observation [18] of an unquenched SOC in this compound. In this paper, we consider magnetic order and excitations in more detail, with a particular focus on the effects of tetragonal distortion generally present in most perovskites.

II. MODEL HAMILTONIAN

Having in mind a layered perovskite structure of Ca_2RuO_4, we consider a square lattice of t_{2g}^4 ions which are assumed to have a low-spin configuration with spin $S=1$ and orbital $L=1$ moments. Intraionic SOC generates three levels at energies $0,\lambda,$ and 3λ, corresponding to the spin-orbit multiplets with total angular momentum $\tilde{S}=0,1,$ and 2. We neglect the highest $\tilde{S}=2$ multiplet at energy 3λ; this is justified if the exchange interactions are not too strong compared to the SOC parameter λ. The remaining ionic degrees of freedom include ground-state singlet $|s\rangle$ and $\tilde{S}=1$ triplet $|T_{0,\pm1}\rangle$ states. In a $|M_S,M_L\rangle$ basis, the wave functions read $|s\rangle=\frac{1}{\sqrt{3}}(|1,-1\rangle-|0,0\rangle+|-1,1\rangle)$, $|T_0\rangle=\frac{1}{\sqrt{2}}(|1,-1\rangle-|-1,1\rangle)$, $|T_{\pm1}\rangle=\pm\frac{1}{\sqrt{2}}(|\pm1,0\rangle-|0,\pm1\rangle)$. In calculations, the Cartesian components $T_x=\frac{1}{i\sqrt{2}}(T_1-T_{-1})$, $T_y=\frac{1}{\sqrt{2}}(T_1+T_{-1})$, and $T_z=iT_0$ are often more convenient. The tetragonal crystal field splits the triplet level as shown in Fig. 1(a). We note that a positive $\delta>0$ corresponds to compression of the octahedra along the c axis (in a view of the point-charge model), and its

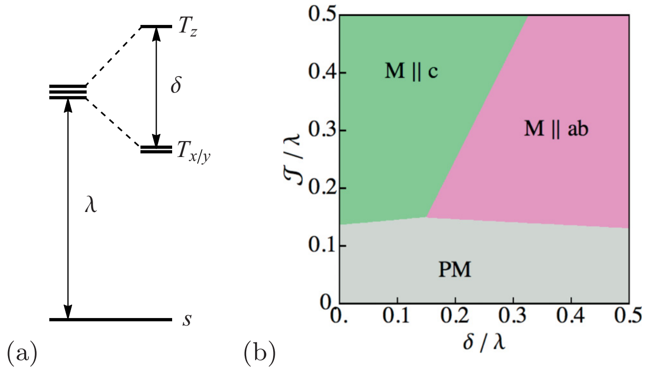

FIG. 1. (Color online) (a) Schematic of spin-orbit level structure including a ground-state singlet and a higher-lying pseudospin $\tilde{S}=1$ triplet; the latter is split by the tetragonal crystal field δ, which favors an in-plane orientation of magnetic moments. (b) Magnetic phase diagram as a function of exchange coupling and crystal-field splitting. It includes a paramagnetic (PM) and two magnetic states with easy-axis ($M \parallel c$) and easy-plane ($M \parallel ab$) orderings.

value is equal to the half of the tetragonal splitting between xy and xz/yz orbital levels, $\delta = (E_{xz/yz} - E_{xy})/2$, which would be expected in the limit of $\lambda = 0$.

The effective singlet-triplet model $\mathcal{H}_{\rm eff}$ that we consider below then reads as follows:

$$\mathcal{H}_{\rm eff} = \mathcal{H}_{\rm CF} + \lambda \sum_i n_i + \mathcal{J} \sum_{<ij>_a} h_{ij}^{(a)} + \mathcal{J} \sum_{<ij>_b} h_{ij}^{(b)}, \quad (1)$$

comprising a tetragonal crystal-field contribution

$$\mathcal{H}_{\rm CF} = \delta \sum_i \left(n_{iz} - \frac{1}{3} n_i \right), \quad (2)$$

a spin-orbit-coupling energy λ of triplet states [second term in Eq. (1)], and, finally, the superexchange interactions [last two terms in Eq. (1)]. For the a-type bonds of the square lattice, the interactions can be represented via the hard-core T bosons as follows [19]:

$$h_{ij}^{(a)} = \boldsymbol{T}_i^{\dagger} \cdot \boldsymbol{T}_j - \tfrac{1}{3} T_{i,x}^{\dagger} T_{j,x} - \tfrac{5}{6} \boldsymbol{T}_i \cdot \boldsymbol{T}_j + \tfrac{1}{6} T_{i,x} T_{j,x} + \text{H.c.} \quad (3)$$

Interactions $h_{ij}^{(b)}$ on b bonds are obtained by the substitution $T_{i,x} \rightarrow T_{i,y}$. In the above equations, $n = n_x + n_y + n_z$, with $n_\alpha = T_\alpha^\dagger T_\alpha$, and $\mathcal{J} = \frac{t_0^2}{U}$ represents the exchange energy scale. Note that $h^{(a,b)}$ represent the quadratic terms in T-boson interactions; the full exchange Hamiltonian also contains three- and four-boson terms [20] which are neglected here. This approximation is valid near the critical points when the density of the condensed bosons is small. We note finally that T operators physically correspond to the singlet-triplet transitions between the $\tilde{S}=0$ and $\tilde{S}=1$ levels. In other words, they are composite objects subject to the hard-core constraint $n_T \leqslant 1$ and can alternatively be represented as $\boldsymbol{T} \rightarrow s^\dagger \boldsymbol{t}$ via singlet s and triplet $\boldsymbol{t}$ particles that obey the constraint $n_s + n_t = 1$.

III. GROUND-STATE PROPERTIES

Depending on the relative strength of the exchange $\mathcal{J}$ and SOC λ parameters, the ground state of effective Hamiltonian (1) can be either paramagnetic or antiferromagnetic. There are two different magnetic phases, with out-of-plane $M \parallel c$ and in-plane $M \parallel ab$ orientations of the staggered moments. The M orientation is decided by the competition between the exchange $\mathcal{J}$ and the crystal-field δ couplings. We calculate below classical energies of magnetically ordered states and obtain from them a phase diagram and ordered moment values.

A. Phase diagram

Magnetic phase I ($M \parallel c$). This state is obtained by a condensation of the T_z component of the $\tilde{S}=1$ triplet: $T_z \rightarrow \sqrt{\rho}_1$. The corresponding classical energy gain is

$$E_{g1} = -\rho_1 \mu_1 = -\frac{1}{4\kappa_1}(\kappa_1 - \beta_1)^2, \quad (4)$$

where $\rho_1 = \frac{1}{2}(1 - \frac{\beta_1}{\kappa_1})$ is the condensate density and $\mu_1 = \frac{1}{2}(\kappa_1 - \beta_1)$. We note that the constant $-\mu$ has a physical meaning of the chemical potential. The condensate density and hence the magnetic moments are determined by the interaction parameters $\kappa_1 = \frac{22}{3}\mathcal{J}$ and $\beta_1 = \lambda + \frac{2}{3}\delta$. The magnetic phase transition sets in at $\kappa_1 = \beta_1$ (i.e., when μ_1 becomes zero); this gives the critical value of the exchange constant $\mathcal{J}$ as $\mathcal{J}_1^c = (3\lambda + 2\delta)/22$.

Magnetic phase II ($M \parallel ab$). The magnetic moment is in the ab plane corresponding to the condensation of $T_x \rightarrow \sqrt{\rho}_2$. The ground-state energy can be represented in the form above,

$$E_{g2} = -\rho_2 \mu_2 = -\frac{1}{4\kappa_2}(\kappa_2 - \beta_2)^2, \quad (5)$$

but with different parameters: $\rho_2 = \frac{1}{2}(1 - \frac{\beta_2}{\kappa_2})$ and $\mu_2 = \frac{1}{2}(\kappa_2 - \beta_2)$, where $\kappa_2 = \frac{19}{3}\mathcal{J}$ and $\beta_2 = \lambda - \frac{1}{3}\delta$. The magnetic phase transition line is given by $\kappa_2 = \beta_2$, and the critical value $\mathcal{J}_2^c = (3\lambda - \delta)/19$.

Using the above results, we find a phase diagram as shown in Fig. 1(b). At small crystal fields δ, the exchange anisotropy terms in Eq. (3) select the out-of-plane M direction. However, already quite small tetragonal splitting δ stabilizes the in-plane magnetic order, which corresponds to the case of Ca_2RuO_4.

B. Staggered magnetization

The magnetic moment of the present singlet-triplet system is represented by the following operator [14]:

$$\boldsymbol{M} = -i\sqrt{6}(\boldsymbol{T} - \boldsymbol{T}^\dagger) - i g_J (\boldsymbol{T}^\dagger \times \boldsymbol{T}), \quad (6)$$

with $g_J = 1/2$. In magnetic phases with condensed bosons, the first term of this operator obtains a finite expectation value [at the ordering wave vector (π,π)]. Using the above results for condensate amplitudes, we find that the staggered magnetic moment in phase I is

$$M_1 = \sqrt{6(1 - \eta_1)}\,, \qquad \mathcal{J} > \mathcal{J}_1^c\,, \quad (7)$$

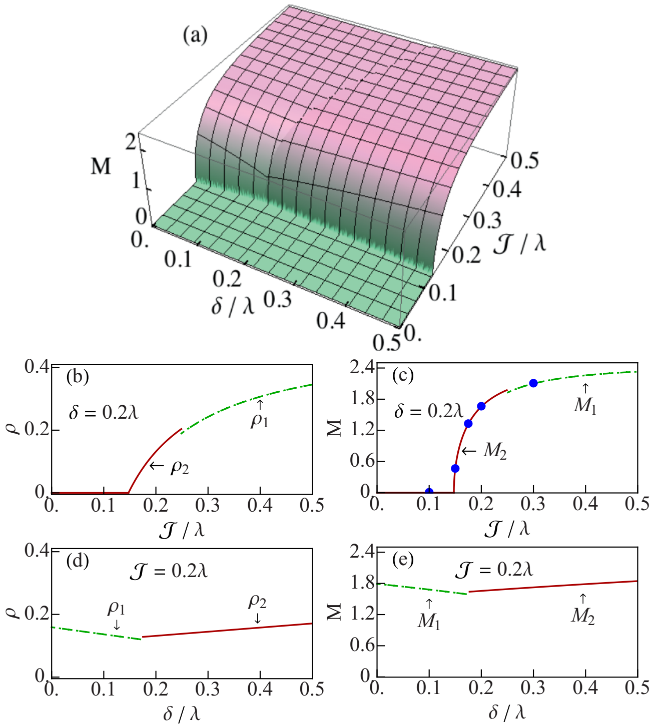

FIG. 2. (Color online) (a) The staggered magnetic moment M as a function of δ and $\mathcal{J}$. (b) The condensate density ρ and (c) the staggered moment M values vs exchange coupling $\mathcal{J}$ for fixed crystal-field splitting $\delta = 0.2\lambda$. [The blue dots in (c) will be referred to later in Fig. 6]. (d) The condensate density ρ and (e) the staggered moment M values vs δ for fixed $\mathcal{J} = 0.2\lambda$.

where $\eta_1 = \beta_1^2/\kappa_1^2$. The same equation holds for the magnetic moment in phase II, but with $\eta_2 = \beta_2^2/\kappa_2^2$ and $\mathcal{J} > \mathcal{J}_2^c$. Parameters $\beta_{1,2}$ and $\kappa_{1,2}$ have been given above.

The numerical results for the staggered moment as a function of parameters δ and $\mathcal{J}$ are shown in Fig. 2. A clear trace of the phase transition from PM to magnetic phases and a discontinuous spin-reorientation transition between phases I and II are observed.

Condensate densities [Fig. 2(b)] and staggered moments [Fig. 2(c)] critically depend on the $\mathcal{J}/\lambda$ ratio. However, they are not sensitive to the value of the anisotropy parameter δ [Figs. 2(d) and 2(e)], whose major effect is the stabilization of phase II with in-plane magnetic moments.

IV. EXCITATION SPECTRA

A. Magnon dispersions

We consider now spin excitations above the ground state. Technically, we follow earlier studies [21,22] which extended a linear spin-wave theory to singlet-triplet models. We handle the particle-number constraint on average only, neglecting magnon interaction effects.

Within this approximation, spin excitations in the paramagnetic phase follow directly from Eqs. (1)–(3), after the Bogoliubov transformation of the T operators (in momentum space). For the T_z component, this gives

$$\omega_z(\boldsymbol{k}) = \left(\lambda + \frac{2}{3}\delta\right)\sqrt{1 + a_z\phi_{\boldsymbol{k}}}, \quad a_z = \frac{22\mathcal{J}}{3\lambda + 2\delta}\,, \tag{8}$$

where $\phi_{\boldsymbol{k}} = \frac{1}{2}(\cos k_x + \cos k_y)$ is a square-lattice form factor. Because of tetragonal symmetry, the T_x and T_y modes are degenerate:

$$\omega_{x/y}(\boldsymbol{k}) = \left(\lambda - \frac{1}{3}\delta\right)\sqrt{1 + a_{x/y}\phi_{\boldsymbol{k}}}\ ,\ a_{x/y} = \frac{19\mathcal{J}}{3\lambda - \delta}\ . \tag{9}$$

For the antiferromagnetically ordered phases, we introduce two sublattices labeled by A and B. It is convenient also to introduce the sublattice-dependent phase shifts $T_{\mathrm{A}} \to iT$, $T_{\mathrm{B}} \to -iT$ and to work within the extended Brillouin zone (BZ). Then, after the Fourier transformation $\boldsymbol{T}_k = \sum_i e^{-i\boldsymbol{k}\cdot\boldsymbol{r}_i}\boldsymbol{T}_i$ in Eqs. (1)–(3), we arrive at the following momentum-space Hamiltonian:

$$\begin{aligned}\mathcal{H} &= \sum_k \left(\mathcal{H}_k^z + \mathcal{H}_k^x + \mathcal{H}_k^y\right)\\ &= \sum_k \left(\lambda + \frac{2}{3}\delta - 4\mathcal{J}\phi_{\boldsymbol{k}}\right)T^\dagger_{\boldsymbol{k},z}T_{\boldsymbol{k},z} - \frac{5}{3}\mathcal{J}\phi_{\boldsymbol{k}}(T_{\boldsymbol{k},z}T_{\boldsymbol{k},z} + \mathrm{H.c.})\\ &\quad + \left[\left(\lambda - \frac{1}{3}\delta + \frac{10}{3}\mathcal{J}\phi_{\boldsymbol{k}}\right)T^\dagger_{\boldsymbol{k},x}T_{\boldsymbol{k},x}\right.\\ &\quad \left. - \frac{3}{2}\mathcal{J}\phi_{\boldsymbol{k}}(T_{\boldsymbol{k},x}T_{\boldsymbol{k},x} + \mathrm{H.c.})\right] + [x \to y]. \end{aligned} \tag{10}$$

Magnetic order in singlet-triplet models implies condensation of a particular component of the triplet state; that is, it mixes up coherently with the ground-state singlet. In order to describe this process, we introduce $\boldsymbol{T} \to s^\dagger\boldsymbol{t}$, with $n_s + n_t = 1$, and transform the basis as follows:

$$\begin{aligned} t_\alpha &= \tilde{s}\sin\theta + \tilde{t}_\alpha\cos\theta,\\ s &= \tilde{s}\cos\theta - \tilde{t}_\alpha\sin\theta, \end{aligned} \tag{11}$$

where $\alpha = z$ (x) for phase I (II). A new $\tilde{s}$ boson is then condensed. Fluctuations of $\tilde{t}_\alpha$ represent amplitude fluctuations, while the two remaining (uncondensed) components of the triplet become transverse magnons. The basis-rotation angle θ is determined by minimization of the classical energy E_g of Hamiltonian (10), which results in $\sin\theta = \sqrt{\rho}$ and $E_g = -\rho\mu$, with condensate densities $\rho_{1,2}$ and potentials $-\mu_{1,2}$ for phases I and II, respectively, as given in a previous Sec. III A.

We consider first magnetic phase I. After the above transformations, the quadratic part of the Hamiltonian (10) takes the following form:

$$\mathcal{H}_k^z = \mathcal{A}_k^z\,\tilde{t}^\dagger_{\boldsymbol{k},z}\tilde{t}_{\boldsymbol{k},z} + \tfrac{1}{2}\mathcal{B}_k^z(\tilde{t}_{\boldsymbol{k},z}\tilde{t}_{-\boldsymbol{k},z} + \mathrm{H.c.}), \tag{12}$$

where

$$\begin{aligned} \mathcal{A}_k^z &= \kappa_1\left[1 + \frac{\phi_{\boldsymbol{k}}}{22}(1 + 11\eta_1)\right],\\ \mathcal{B}_k^z &= \kappa_1\left[\frac{\phi_{\boldsymbol{k}}}{22}(1 - 11\eta_1)\right]. \end{aligned} \tag{13}$$

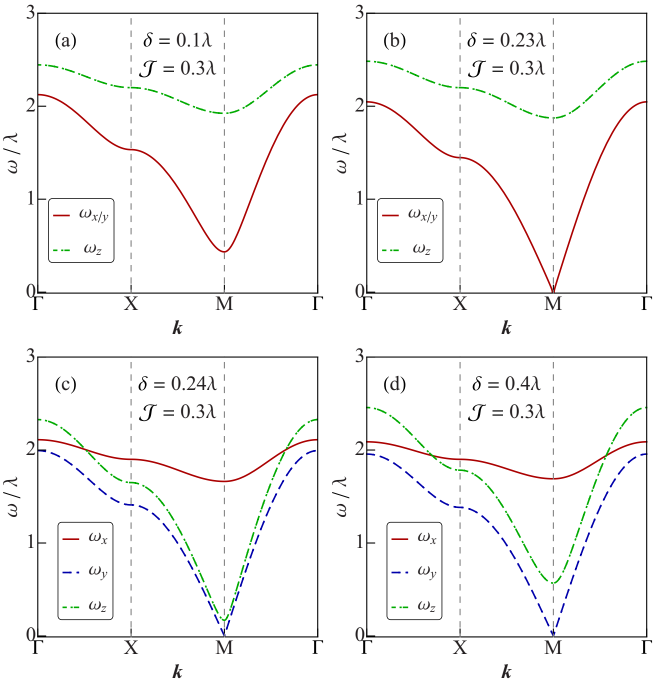

FIG. 3. (Color online) The excitation energies ω_α (in units of SOC constant λ) vs momentum $\boldsymbol{k}$ for fixed $\mathcal{J} = 0.3\lambda$ and different δ values: (a) $\delta = 0.1\lambda$, (b) $\delta = 0.23\lambda$, (c) $\delta = 0.24\lambda$, and (d) $\delta = 0.3\lambda$. (a) and (b) represent phase I, and (c) and (d) represent phase II. Here, $\Gamma = (0,0)$, $X = (0,\pi)$, and $M = (\pi,\pi)$.

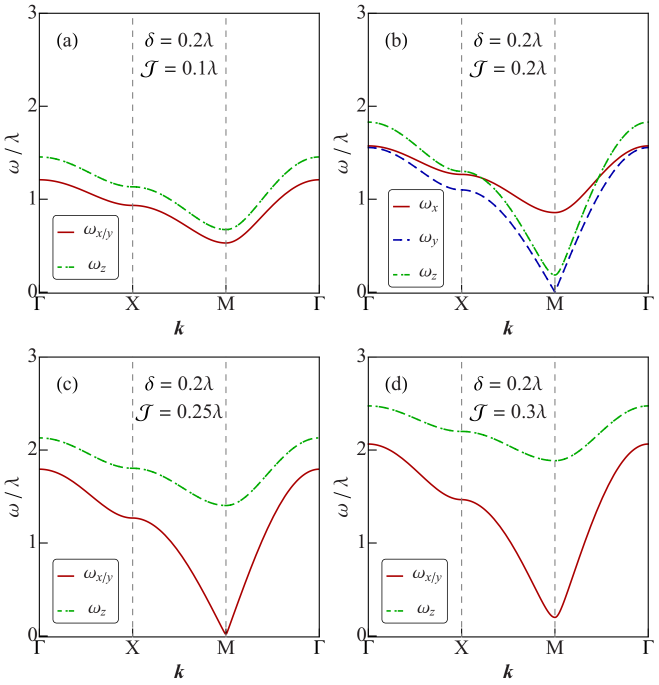

FIG. 4. (Color online) The same as the Fig. 3, but for fixed $\delta = 0.2\lambda$ and different $\mathcal{J}$ values: (a) $\mathcal{J} = 0.1\lambda$, (b) $\mathcal{J} = 0.2\lambda$, (c) $\mathcal{J} = 0.25\lambda$, and (d) $\mathcal{J} = 0.3\lambda$. (a) corresponds to the paramagnetic phase, (b) represents phase II, and (c) and (d) represent phase I.

Diagonalization of Eq. (12) gives the amplitude mode dispersion:

$$\omega_z(\boldsymbol{k}) = \sqrt{\left(\mathcal{A}^z_k - \mathcal{B}^z_k\right)\left(\mathcal{A}^z_k + \mathcal{B}^z_k\right)} = \sqrt{\kappa_1^2 + \beta_1^2\phi_{\boldsymbol{k}}}\,. \tag{14}$$

The transverse components $t_{x/y}$ are degenerate in phase I. Accounting for the chemical energy shift $-\mu(n_x + n_y)$, we find the corresponding quadratic Hamiltonian for x/y modes in the form of Eq. (12) again, with the following constants:

$$\begin{aligned} \mathcal{A}^x_k &= \mathcal{A}^y_k = \bar{\kappa}_1 - \delta + \frac{5}{11}\bar{\kappa}_1\phi_{\boldsymbol{k}}, \\ \mathcal{B}^x_k &= \mathcal{B}^y_k = \frac{9}{22}\bar{\kappa}_1\phi_{\boldsymbol{k}}, \end{aligned} \tag{15}$$

where $\bar{\kappa}_1 = (\kappa_1 + \beta_1)/2$. This gives spin-wave dispersions

$$\omega_{x/y}(\boldsymbol{k}) = (\bar{\kappa}_1 - \delta)\sqrt{1 + \frac{19}{22}\frac{\bar{\kappa}_1\phi_{\boldsymbol{k}}}{(\bar{\kappa}_1 - \delta)}} \tag{16}$$

for magnetic phase I with $M \parallel c$.

For magnetic phase II, similar calculations give the following results for the energy-momentum dispersions of the amplitude (x) and transverse (y,z) modes:

$$\begin{aligned} \omega_x(\boldsymbol{k}) &= \sqrt{\kappa_2^2 + \beta_2^2\phi_{\boldsymbol{k}}}\,, \\ \omega_y(\boldsymbol{k}) &= \bar{\kappa}_2\sqrt{1 + \phi_{\boldsymbol{k}}}\,, \\ \omega_z(\boldsymbol{k}) &= (\bar{\kappa}_2 + \delta)\sqrt{1 + \frac{22}{19}\frac{\bar{\kappa}_2\phi_{\boldsymbol{k}}}{(\bar{\kappa}_2 + \delta)}}\,. \end{aligned} \tag{17}$$

It is noticed that in phase II with $M \parallel ab$, there is no degeneracy of magnon branches, i.e., in-plane (y) and out-of-plane (z) magnons are split.

Some examples of magnon dispersion curves, representing different magnetic phases, are plotted in Figs. 3 and 4. Figure 3 shows the evolution of excitation spectra as a function of the crystal-field parameter δ, and their dependence on the exchange parameter $\mathcal{J}$ is illustrated in Fig. 4. The features mentioned above such as the separation of the amplitude mode from the low-energy magnon modes and splitting of the latter into two distinct branches in phase II can be noticed.

In order to see the evolution of the magnon gaps in more detail, we plot in Fig. 5 the magnetic excitation energies at the Bragg point $\boldsymbol{Q} = (\pi,\pi)$ as a function of the exchange constant $\mathcal{J}$ at different δ values. In the PM phase (small $\mathcal{J}$), all the branches have a finite gap. At the critical value of $\mathcal{J}$, the gap for the amplitude mode closes. A further increase of $\mathcal{J}$ enhances the excitation gaps for all the branches in phase I [see Fig. 5(a)]. In phase II, there remains a gapless Goldstone mode [see Figs. 5(b)–5(d)], corresponding to a free rotation of the staggered moment within the *ab* plane. Figures 5(b) and 5(c) illustrate a transformation of spin-wave dispersions at the first-order phase transitions between phases I and II.

B. Magnon intensities

The intensity of spin excitations is given by the imaginary part of the dynamic spin susceptibility, which, within the present linear spin-wave approximation, takes the following

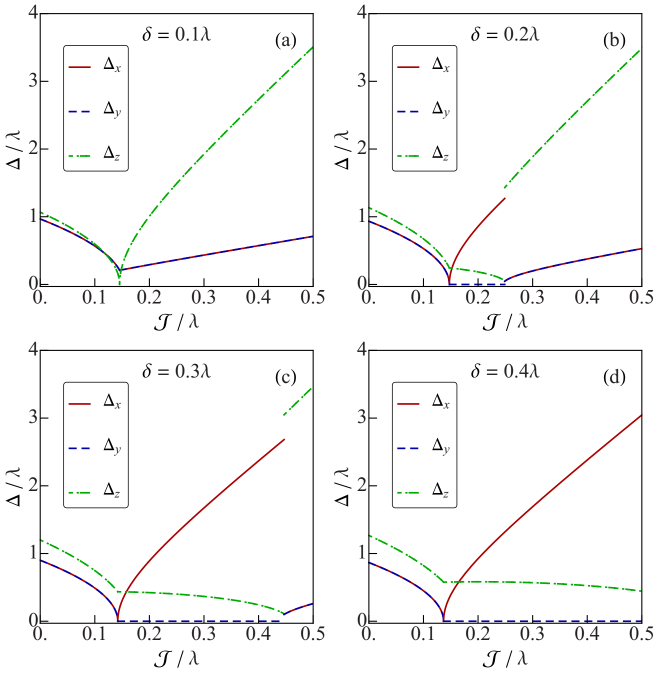

FIG. 5. (Color online) The excitation energy gaps at the Bragg (M) point, $\Delta = \omega(\boldsymbol{Q})$, as a function of exchange interaction $\mathcal{J}$ for different values of the crystal-field parameter: (a) $\delta = 0.1\lambda$, (b) $\delta = 0.2\lambda$, (c) $\delta = 0.3\lambda$, and (d) $\delta = 0.4\lambda$.

form:

$$\mathrm{Im}\chi_{\mathbf{q}}^{\gamma}(\omega) = \frac{|\, F_{\gamma}(\boldsymbol{q})\, |}{\omega_{\gamma}(\boldsymbol{q})}\, \delta(\omega - \omega_{\gamma}(\boldsymbol{q})). \tag{18}$$

In the paramagnetic phase, the factors $F_{\gamma}(\boldsymbol{q})$ representing the spectral weights of $\gamma = x,y,z$ magnon modes are given by

$$F_x(\boldsymbol{q}) = F_y(\boldsymbol{q}) = \frac{54\bar{\kappa}_2}{19}\phi_{\boldsymbol{q}}, \quad F_z(\boldsymbol{q}) = \frac{30\bar{\kappa}_1}{11}\phi_{\boldsymbol{q}}. \tag{19}$$

In magnetic phase I, we have

$$\begin{aligned} F_x(\boldsymbol{q}) = F_y(\boldsymbol{q}) &= \frac{27\bar{\kappa}_1}{11}\phi_{\boldsymbol{q}}, \\ F_z(\boldsymbol{q}) &= \frac{3\bar{\kappa}_1}{11}(-1 + 11\eta_1)\phi_{\boldsymbol{q}}, \end{aligned} \tag{20}$$

and finally, for magnetic phase II, we obtain

$$\begin{aligned} F_x(\boldsymbol{q}) &= \frac{3\bar{\kappa}_2}{19}(-1 + 19\eta_2)\phi_{\boldsymbol{q}}, \\ F_y(\boldsymbol{q}) &= \frac{54\bar{\kappa}_2}{19}\phi_{\boldsymbol{q}}, \\ F_z(\boldsymbol{q}) &= \frac{60\bar{\kappa}_2}{19}\phi_{\boldsymbol{q}}. \end{aligned} \tag{21}$$

Magnon intensities are given by $I(\mathbf{q},\omega) = \sum_{\gamma} \mathrm{Im}\chi_{\mathbf{q}}^{\gamma}(\omega)$. The contour plots of this quantity, multiplied by $\sqrt{\omega}$ for clarity, are shown in Fig. 6. In the ($\mathcal{J} - \delta$) parameter space, five different panels correspond to the blue points in Fig. 2(c) and thus represent the paramagnetic phase [Fig. 6(a)], magnetic phase II [$M \parallel ab$; Figs. 6(b)–6(d)], and, finally, magnetic phase I [$M \parallel c$; Fig. 6(e)].

In the PM phase, the intensities of all (degenerate x/y and z) modes are nearly equal. In phase II [Figs. 6(b)–6(d)], which is of particular interest in the context of $\mathrm{Ca_2RuO_4}$, the intensity of the highest-energy (amplitude) mode is large near the critical point [see inset in Fig. 6(b)], but it fades away rather quickly at larger $\mathcal{J}$ values.

V. APPLICATION TO $\mathrm{Ca_2RuO_4}$

Calcium ruthenate ($\mathrm{Ca_2RuO_4}$) has a layered perovskite structure similar to that of $\mathrm{La_2CuO_4}$ cuprate and shows a Mott-insulating behavior below room temperature [23,24]. It undergoes a magnetic phase transition at ∼110 K, below which an antiferromagnetic order with a staggered moment $M \simeq 1.3\mu_{\mathrm{B}}$ is observed [25]. A sizable value of the LS product indicates that SOC is not quenched [18], and hence this material may exhibit some features of the “excitonic” magnetism considered above. To our knowledge, no dynamical spin susceptibility measurements for $\mathrm{Ca_2RuO_4}$ have been reported to date; some theoretical expectations are given below.

The observed ab-plane orientation of the moments [25] is consistent with phase II in Fig. 1(b), which is stabilized by a compressive tetragonal distortion present in $\mathrm{Ca_2RuO_4}$.

One can roughly estimate the parameters $\mathcal{J}/\lambda$ and δ/λ from the observed staggered moment $M \simeq 1.3\mu_{\mathrm{B}}$ [25] and the static magnetic susceptibility $\chi \simeq 2.6 \times 10^{-3}$ emu/mol [25].

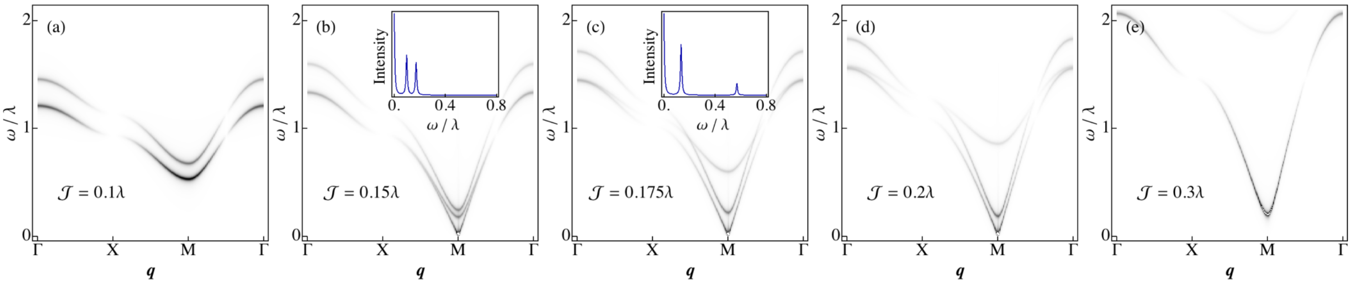

FIG. 6. (Color online) Contour maps of the magnon intensities (multiplied by $\sqrt{\omega}$ for better visibility), $\sqrt{\omega}\, I(\mathbf{q},\omega) = \sqrt{\omega}\, \mathrm{Im}\chi_{\mathbf{q}}(\omega)$, for constant $\delta = 0.2\lambda$ and different values of $\mathcal{J}$: (a) $\mathcal{J} = 0.1\lambda$, (b) $\mathcal{J} = 0.15\lambda$, (c) $\mathcal{J} = 0.175\lambda$, (d) $\mathcal{J} = 0.2\lambda$, and (e) $\mathcal{J} = 0.3\lambda$. Note that (a) belongs to paramagnetic phase, (b)–(d) represent magnetic phase II, and (e) represents magnetic phase I [see the blue points in Fig. 2(c)]. The insets in (b) and (c) show a direct comparison of the intensities $I(\mathbf{Q},\omega)$ of three modes at the ordering wave vector (M point). The highest peak corresponds to the amplitude mode, the middle one represents an out-of-plane magnon, and the lowest peak is an in-plane magnon (which is gapless and hence not properly shown for numerical reasons).

The moment M is determined by η_2 [see Eq. (7)], defining the distance to the critical point, while the susceptibility is given by

$$\chi_{ab} = \frac{12\mu_B^2 N_A}{\kappa_2(1+\eta_2)} , \qquad (22)$$

where N_A is Avogadro's number. From the M and χ equations, we find $\eta_2 \simeq 0.85$ and estimate the parameters $\mathcal{J}/\lambda \sim 0.17$ and $\delta/\lambda \sim 0.2$. Magnon dispersions in Ca_2RuO_4 are then expected to resemble the plots shown in Figs. 6(b) and 6(c). These plots suggest a full magnon bandwidth of the order of $1.5\lambda \sim 100$ meV, given a spin-orbit-coupling constant $\lambda\ (= \xi/2) \simeq 75$ meV [18]. The parameter $\mathcal{J} = \frac{t_0^2}{U} \simeq 13$ meV which follows from these estimates seems reasonable for t_{2g} systems with $t_0 \sim 0.2$ eV and $U \sim 3$ eV. As far as the amplitude mode is concerned, the insets in Fig. 6 suggest sizable intensities; however, it might be difficult to identify this mode because it falls in the phonon-energy window (∼40 meV).

VI. SUMMARY

We have studied here the phase diagram and magnetic excitations in Van Vleck–type d^4 Mott insulators with a spin-orbit singlet ground state. As the intersite exchange interactions increase, the system makes a transition into an antiferromagnetically ordered state. For the square-lattice geometry considered here, the exchange anisotropy supports a uniaxial-type magnetic order. Under compressive strain, this order changes to the easy-plane one via a first-order phase transition. We have calculated magnetic excitations over an entire phase diagram, quantifying the magnon dispersions and their intensities. We hope that the results presented here will motivate experimental studies of Ca_2RuO_4 and other potential candidate materials for excitonic-type magnetism [26] by means of inelastic neutron and/or resonant x-ray scattering techniques.

ACKNOWLEDGMENT

We would like to thank B. J. Kim for useful discussions.

[1] K. I. Kugel and D. I. Khomskii, Sov. Phys. Usp. **25**, 231 (1982).
[2] G. Khaliullin and S. Maekawa, Phys. Rev. Lett. **85**, 3950 (2000).
[3] G. Khaliullin, Prog. Theor. Phys. Suppl. **160**, 155 (2005).
[4] R. J. Elliott and M. F. Thorpe, J. Appl. Phys. **39**, 802 (1968).
[5] G. Jackeli and G. Khaliullin, Phys. Rev. Lett. **102**, 017205 (2009).
[6] J. Chaloupka, G. Jackeli, and G. Khaliullin, Phys. Rev. Lett. **105**, 027204 (2010); **110**, 097204 (2013).
[7] G.-W. Chern and N. Perkins, Phys. Rev. B **80**, 180409(R) (2009).
[8] G. Chen and L. Balents, Phys. Rev. B **84**, 094420 (2011).
[9] B. J. Kim, H. Jin, S. J. Moon, J.-Y. Kim, B.-G. Park, C. S. Leem, J. Yu, T. W. Noh, C. Kim, S.-J. Oh, J.-H. Park, V. Durairaj, G. Cao, and E. Rotenberg, Phys. Rev. Lett. **101**, 076402 (2008).
[10] B. J. Kim, H. Ohsumi, T. Komesu, S. Sakai, T. Morita, H. Takagi, and T. Arima, Science **323**, 1329 (2009).
[11] J. Kim, D. Casa, M. H. Upton, T. Gog, Y.-J. Kim, J. F. Mitchell, M. van Veenendaal, M. Daghofer, J. van den Brink, G. Khaliullin, and B. J. Kim, Phys. Rev. Lett. **108**, 177003 (2012).
[12] W. Witczak-Krempa, G. Chen, Y. B. Kim, and L. Balents, Annu. Rev. Condens. Matter Phys. **5**, 57 (2014).
[13] A. Abragam and B. Bleaney, *Electron Paramagnetic Resonance of Transition Ions* (Clarendon, Oxford, 1970).
[14] G. Khaliullin, Phys. Rev. Lett. **111**, 197201 (2013).
[15] T. M. Holden, W. J. L. Buyers, E. C. Svensson, R. A. Cowley, M. T. Hutchings, D. Hukin, and R. W. H. Stevenson, J. Phys. C: Solid State Phys. **4**, 2127 (1971).
[16] W. J. L. Buyers, T. M. Holden, E. C. Svensson, R. A. Cowley, and M. T. Hutchings, J. Phys. C: Solid State Phys. **4**, 2139 (1971).
[17] T. Giamarchi, Ch. Rüegg, and O. Tchernyshyov, Nat. Phys. **4**, 198 (2008).
[18] T. Mizokawa, L. H. Tjeng, G. A. Sawatzky, G. Ghiringhelli, O. Tjernberg, N. B. Brookes, H. Fukazawa, S. Nakatsuji, and Y. Maeno, Phys. Rev. Lett. **87**, 077202 (2001).
[19] Alternatively, one can represent Eq. (3) also in terms of real fields $\mathbf{u}$ and $\mathbf{v}$, defined as $\mathbf{T} = \mathbf{u} + i\mathbf{v}$ [14]. In the $\mathbf{u} - \mathbf{v}$ representation, Eq. (3) coincides with the corresponding quadratic part of the exchange Hamiltonian (2) of Ref. [14]. We also note that Ref. [14] has further replaced the bond-dependent terms by their average [see Eq. (3) of Ref. [14]]; we do not use that approximation here.
[20] See the second and third lines in Eq. (2) of Ref. [14].
[21] T. Sommer, M. Vojta, and K. W. Becker, Eur. Phys. J. B **23**, 329 (2001).
[22] M. Matsumoto, B. Normand, T. M. Rice, and M. Sigrist, Phys. Rev. B **69**, 054423 (2004).
[23] S. Nakatsuji, S. Ikeda, and Y. Maeno, J. Phys. Soc. Jpn. **66**, 1868 (1997).
[24] G. Cao, S. McCall, M. Shepard, J. E. Crow, and R. P. Guertin, Phys. Rev. B **56**, R2916 (1997).
[25] M. Braden, G. André, S. Nakatsuji, and Y. Maeno, Phys. Rev. B **58**, 847 (1998).
[26] G. Cao, T. F. Qi, L. Li, J. Terzic, S. J. Yuan, L. E. DeLong, G. Murthy, and R. K. Kaul, Phys. Rev. Lett. **112**, 056402 (2014).